Wake-tracking and turbulence modelling in computational aerodynamics of wind turbine aerofoils

M S Campobasso[1], **A Zanon**[2], **E Minisci**[1], and **A Bonfiglioli**[3]*
[1]Department of Aerospace Engineering, James Watt Building South, Glasgow University, Glasgow, UK
[2]Dipartimento di Energetica e Macchine, Universita' di Udine, Udine, Italy
[3]Dipartimento di Ingegneria e Fisica dell'Ambiente, Universita' della Basilicata, Potenza, Italy

The manuscript was received on 19 March 2009 and was accepted after revision for publication on 28 May 2009.

DOI: 10.1243/09576509JPE778

Abstract: This article addresses two modelling aspects of wind turbine aerofoil aerodynamics based on the solution of the Reynolds-averaged Navier–Stokes (RANS) equations. One of these is the effect of an *a priori* method for structured grid adaptation aimed at improving the wake resolution. The presented results emphasize that the proposed adaptation strategy greatly improves the wake resolution in the far field, whereas the wake is completely diffused by the non-adapted grid with the same number and spacing patterns of grid nodes. The proposed adaptation approach can be easily included in the structured generation process of both commercial and in-house-structured mesh generators.

The other numerical aspect examined herein is the impact of particular choices for turbulence modelling on the predicted solution. This includes the comparative analysis of numerical solutions obtained by using different turbulence models, and also aims at quantifying the solution inaccuracy arising from not modelling the laminar-to-turbulent transition. It is found that the drag forces obtained by considering the flow as transitional or fully turbulent may differ by 50 per cent.

All these issues are investigated using a special-purpose hyperbolic grid generator and two multi block structured finite volume RANS codes. The numerical experiments consider the flow field past a wind turbine aerofoil for which an exhaustive campaign of steady and unsteady experimental measurements was conducted. The predictive capabilities of the CFD solvers are validated by comparing experimental data and numerical predictions for selected flow regimes. The incompressible analysis and design code XFOIL is also used to support the findings of the comparative analysis of numerical RANS-based results and experimental data.

Keywords: wake-tracking, turbulence modelling, grid generation, wind turbine aerodynamics, Reynolds-averaged Navier-Stokes, computational fluid dynamics

1 INTRODUCTION

Improving the steady and unsteady aerodynamic performance of existing wind turbines (WTs) and designing the next generation of more powerful and more reliable machines will increasingly require the use of high-fidelity aerodynamic models such as those of computational fluid dynamics (CFD), and also a substantial enhancement of the level of confidence in the potential of this technology.

Outstanding studies on the current capabilities of CFD to predict the steady and unsteady aerodynamics of WT aerofoil have appeared in the past few years [**1**–**3**], but the level of public domain knowledge and experience in this area is still significantly lower than that in related fields, such as aircraft wing or turbomachinery blade computational aerodynamics.

One of the crucial phases in the classical design of new WT blades is the accurate prediction of the

**Corresponding author: Environmental Engineering and Physics, University of Basilicata, Viale Ateneo Lucano 10, Potenza 85100, Italy.*
email: aldo.bonfiglioli@unibas.it

aerodynamic force coefficients of their aerofoils. These aerodynamic coefficients can then be used to calculate the force acting on the blades at each radius, and the radial integral of such forces determines both the overall torque (and thus the power) available at the shaft of the alternator and the axial thrust acting on the turbine, which is needed to size the tower and its support.

The use of CFD codes solving the Reynolds-averaged Navier–Stokes (RANS) equations is emerging as a viable option to accomplish these objectives. However, their employment in WT aerodynamics presents several important challenges. Some of these arise because the flow field past the blade is transitional over a significant portion of the blade height. Indeed, the Reynolds number decreases dramatically from tip to hub, and the highest value occurring at the tip is often close to the upper end of the transitional region. The Mach number also varies substantially along the blade, being always in the low subsonic range and achieving extremely low levels at the hub.

These features point to the necessity of suitably accounting for laminar-to-turbulent transition, and also for incompressibility effects when existing, well-validated, efficient and reliable compressible RANS solvers are to be used for these analyses. One of the first reported studies highlighting the importance of correctly modelling the transition as a prerequisite for obtaining accurate steady-state predictions is reported in reference [**4**] dealing with the prediction of the steady performance of a WT aerofoil. In reference [**5**], it is shown how the use of a transition-modelling algorithm yields remarkable improvements in the prediction of the flow field past the blade of a WT rotor with respect to the case in which the flow is assumed turbulent from the blade leading edge.

As for the effects of incompressibility, a striking example of the low Mach number effects on the prediction of separated aerofoil flows by means of an existing compressible RANS code is reported in reference [**3**]. This article shows that the measured incidence associated with the stall inception of a WT aerofoil can only be reproduced numerically by using a low-speed preconditioner to take into account the incompressibility effects.

An additional factor that may affect the CFD prediction of aerofoil forces is the choice of the turbulence model. The results of Le Pape and Lecanu [**3**], for example, show that the prediction of the flow field past a WT aerofoil with an incidence of 12° does not reveal any flow separation when using the K–ω turbulence model reported in reference [**6**], whereas a heavily stalled flow field (much closer to the experimental observations) is obtained when using the shear stress transport (SST) K–ω model described in reference [**7**].

The aforementioned turbulence model-related issues are crucial if the forces acting on the blade aerofoils are to be determined by means of the so-called *near-field* method, whereby such forces are determined by means of surface integration of local static pressure and viscous stress. This approach is straightforward, but the accuracy of its outcome is heavily affected by the level of numerical dissipation and the truncation error of the numerical discretization (note that both parameters decrease as the grid is refined). Prompted by these issues, particularly that of determining the aerodynamic drag with an approach much less sensitive to the refinement of the grid at hand, however, a *mid-field* approach for the calculation of the aerofoil forces has recently received some attention [**8**]. Starting from a given RANS solution, this method determines the aerofoil forces by performing a volume integral of an entropy-, static pressure- and total enthalpy-dependent function in the boundary layers and the wake regions. The boundary of the domain of integration typically extends two or three chords away from the body. Reported results show that the drag computed with the mid-field approach is much less sensitive to grid refinement than the near-field integration method. The former technique, however, assumes a degree of boundary layers and wake resolution above a minimum threshold.

A high level of wake and shed vorticity resolution is also important in the study of wake–body interaction, such as that leading to the reduction of the power output of a turbine operating in the wake produced by an upstream turbine in a wind farm [**9**]. In the framework of the RANS approach, the technologies one may adopt to enhance the wake resolution keeping the overall size of the computational mesh within acceptable bounds are (a) grid-adaptation [**10**] and (b) high-order methods [**11**].

Given the highlighted necessity of suitably resolving blade wakes, the primary objective of this article is to quantify the accuracy enhancements achievable by using wake-adapted grids (i.e. computational meshes that maximize the resolution of the wake shed by the blade aerofoils), rather than standard meshes that take no account of the flow patterns. The comparative assessment is performed by analysing the flow field past a wind turbine aerofoil computed by means of two structured multi-block RANS codes with both standard and wake-tailored computational grids.

The second thread of this article is the comparative analysis of the effects of turbulence and transition modelling on the predicted flow field and aerofoil characteristics. To this aim, we compare the flow field past the selected aerofoil computed (a) by using the two RANS solvers both with and without transition modelling and (b) by using one RANS solver employing four different turbulence models.

All presented investigations are based on two-dimensional (2D) simulations and measurements of the flow field past the FFA-W3-241 WT aerofoil [**12**], which is depicted in Fig. 1. The numerical simulations have been carried out by means of two different structured finite volume RANS codes: the public

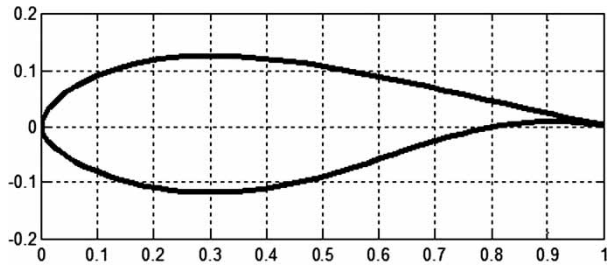

Fig. 1 Profile of FFA-W3-241 aerofoil

domain code ISAAC [**13**] and the commercial code FINE^{TM}/Turbo (http://www.numeca.be/). The predictive capabilities of these RANS codes are assessed by comparing their predictions to the experimental data and the results obtained using XFOIL [**14**], an incompressible 2D analysis and design code that uses a coupled potential flow and integral boundary layer model and a very accurate transition model. More specifically, XFOIL uses an e^N method for transition prediction, and is widely regarded as one of the best tools available for predicting transition on 2D aerofoils. A thorough description of the implementation of the transition model in XFOIL can be found in reference [**15**].

The procedure adopted for the generation of the wake-tailored grid is reported in section 2, whereas a summary of the main features of the two RANS solvers employed in this study is given in section 3. Section 4 presents the comparative analysis of the computed flow past the FFA aerofoil using the standard- and wake-tailored grids, and also highlights the impact of transition modelling on the computed aerodynamic force. The parametric study on the dependence of the computed solution on the turbulence model is summarized in section 5, whereas the main conclusions of these investigations are provided in section 6.

2 GRID GENERATION

The geometry of many families of WT aerofoils consists of an asymmetric profile with a fairly thin and cambered trailing edge (TE), and these features result in a locally concave shape of the lower side. When using a structured RANS solver for the analysis of the flow field past these aerofoils, a C-type grid is typically used for the numerical simulation. In this circumstance, however, the use of a standard C-grid with a straight cut aligned with the aerofoil chord may yield unacceptably poor resolution of the wake. This occurs because in most regions behind the aerofoil, the wake is not aligned with the grid cut, in the neighbourhood of which a very high spatial resolution is available due to the grid line clustering past the aerofoil surface. The wake does not travel in the highly refined strip past the C-cut of a standard grid; conversely, it rapidly departs from it soon after the TE, and it travels in a region of increasingly low refinement. This leads to a premature and unphysical dissipation of the wake, and this occurrence may seriously hinder the use of mid-field methods to calculate the forces acting on the aerofoil. This mechanism also poses serious problems to the use of RANS-based methods for the study of wake–body interactions. For a given order of accuracy of the adopted CFD algorithm, this problem can be solved (a) by increasing the refinement in the wake region, (b) by adapting the geometry of the grid in the wake region to the wake, or (c) by a combination of both actions.

The aim of this section is to present an *a priori* mesh adaptation method aimed at improving the wake resolution of a given C-mesh used for the CFD analysis of WT aerofoils. The technique only varies the local mesh topology, and does not alter the overall number of grid nodes.

The grids adopted in this study have been generated by the structured grid generator WINGRID described in reference [**16**]. The code builds a C-grid past the aerofoil by solving a system of two hyperbolic partial differential equations with an implicit discretization. The grids are orthogonal, and the generation process allows a high degree of control of node stretching and local distance from all boundaries. One of the original features of WINGRID is the possibility of actively controlling the input geometry of the C-cut. Three options are available: (a) straight horizontal cut (aligned with the aerofoil chord), (b) straight cut rotated with respect to the chord direction by a user-given angle, and (c) coordinates of grid-cut geometry provided by the user. As shown in the result section, the grid constructed using the third option yields the best resolution of the flow field past aerofoils with sharp and cambered TE, provided that the user-given cut geometry is a reasonable approximation to the wake trajectory. This occurs because the wake shed by these aerofoils describes a compound trajectory: soon after the TE, the flow is aligned with the aerofoil camber line, and then it takes the free-stream direction within less than one chord length from the TE. The first patch of this pattern is highlighted in Fig. 2, the three sketches of which depict the C-cut obtained by using the three aforementioned options and the TE streamline computed by a RANS calculation for a free-stream direction $\alpha = 4^\circ$. As expected, the straight horizontal cut of option 1 is intersected by the wake, directed downwards at the TE and upwards from about 40 per cent chord lengths to the exit of the computational domain; the straight cut of option 2 rotated by α completely misses the wake because the direction of the C-cut and the wake close to the TE are initially opposite. The user-given cut geometry of option 3 is that which best tracks the wake. The importance of aligning the C-cut and the wake lies in that the maximum grid refinement in the normal direction is concentrated

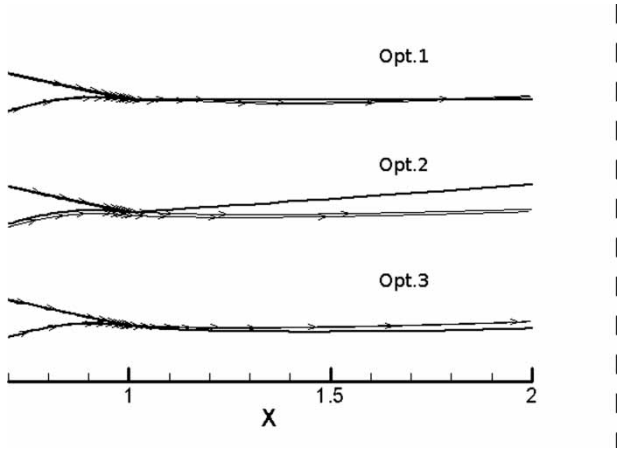

Fig. 2 Geometry option for C-cut construction

around the cut, and therefore the wake–cut alignment guarantees the best wake resolution.

The misalignment of C-cut and wake has negative consequences also further downstream, as illustrated in Figs 3 and 4. The plots report the far-field grid obtained by using options 1 and 3, respectively, and these grids are generated for the CFD analysis of the flow field with a free-stream direction of 10.2°. The computed streamline that emanates from the aerofoil TE is also reported in both figures. One sees (Fig. 3) how the wake rapidly moves to a region with scarce grid refinement in the case of the straight horizontal cut. Conversely, Fig. 4 shows that the computed wake remains in a high-refinement area even in the far-field region, though not exactly in the middle of the maximum refinement band about the C-cut. The wake in Fig. 4 also appears not to be perfectly aligned with the C-cut. These minor mismatches in the near-field region depend on the particular choice

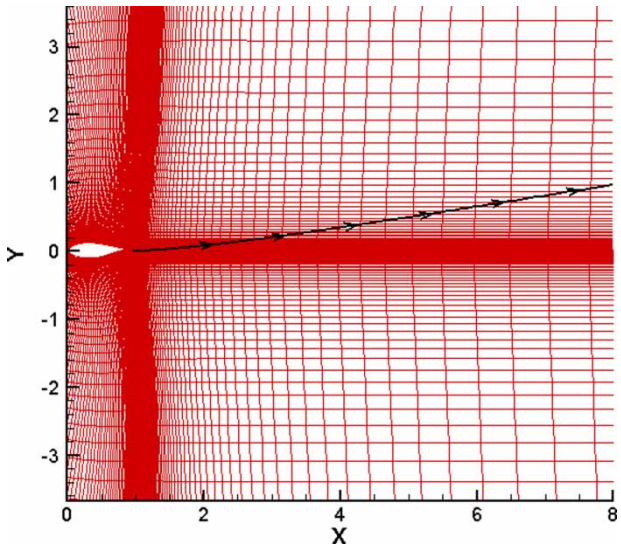

Fig. 3 Enlarged view of C-grid behind aerofoil: straight horizontal C-cut

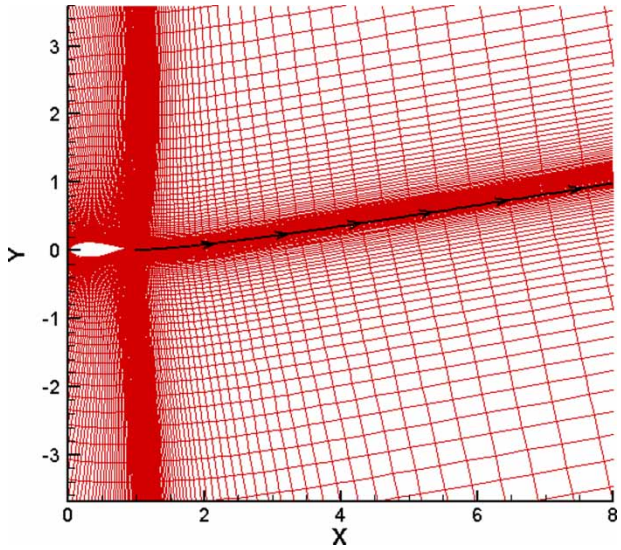

Fig. 4 Enlarged view of C-grid behind aerofoil: adapted C-cut

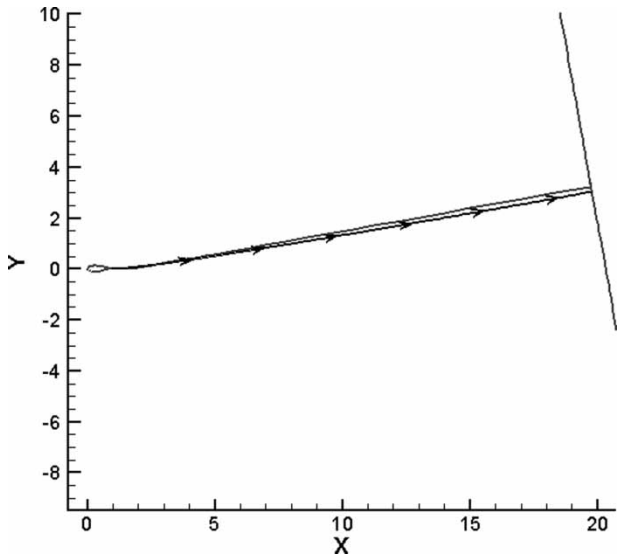

Fig. 5 Wake trajectory and C-cut of wake-adapted grids

of the user-given cut geometry. Further downstream, the computed wake and the C-cut become parallel as shown in Fig. 5.

In the analyses reported herein, the user-given cut profile is generated as follows: for the first chord length behind the TE, one uses the streamline predicted by XFOIL for the given free-stream direction α; a straight line rotated by α is instead used from the end of the XFOIL streamline to the downstream far-field boundary of the C-grid. Since this construction of the C-cut is based on a forecast of the wake trajectory, we call this process an *a priori* grid-adaptation method. Note that the CPU time of a single XFOIL analysis amounts to fractions of a second, making this cost negligible with respect to that required for the grid generation.

The CFD results presented in this article will highlight the substantial differences of flow resolution and convergence property of the CFD solvers achieved by using the adaptive geometry of the cut. It should be noted that the importance of aligning the wake grid with the mid- and far-field wakes had been already recognized, as shown by the multi-block grids used in reference [**17**]. The importance of the following results, however, is to emphasize the necessity of adapting the wake grid also in the TE proximity.

3 CFD CODES

To highlight the generality of the conclusions provided in this article with regard to the accuracy improvements achieved by using the wake resolution approach, we have conducted a large portion of the analyses reported in this article by means of two different 3D structured multi-block RANS solvers, namely the open source code ISAAC and the commercial code FINE^{TM}/Turbo developed by NUMECA International. Both solvers use a finite volume cell-centred scheme to discretize the conservation law form of the compressible flow equations. The conservative flow variables are used as dependent variables by both solvers.

The ISAAC code [**13**] uses a second-order upwind space discretization. Advection terms in the mean flow equations are solved using Roe's approximate Riemann solver coupled with MUSCL extrapolations; an upwind-biased discretization is also used for the convective terms in the turbulence equations, while the viscous terms are calculated with a central difference approximation. Mean flow and turbulence equations are solved in a coupled fashion using an implicit spatially split diagonalized approximate factorization. The multigrid algorithm is also made use of to speed up convergence. The interested reader is referred to reference [**13**] for further details on the algorithmic aspects of ISAAC. As for turbulence modelling, the ISAAC solver features several turbulence closure models, including the K–ω model [**6**], the variant of the K–ε model described in reference [**18**], and an algebraic stress model (ASM) version of both the K–ω and the K–ε models [**19**]. The turbulence models reported in references [**18**] and [**6**] use a linear relationship between the Reynolds stress and the strain rate tensors (Boussinesq approximation), whereas the ASM counterpart of both models features a non-linear algebraic relationship between the components of the Reynolds stress tensor and those of the velocity gradient. The variations of the computed flow field past the FFA-W3-241 aerofoil arising by using these four models are assessed in section 5. Note that all four models are low Reynolds number models, and they can thus be integrated all the way down to viscous walls without requiring wall functions. A feature of the implementation of these models in ISAAC that has been extensively used in this study is the possibility of prescribing the position along the aerofoil sides where transition from laminar to turbulent boundary layer occurs.

The FINE^{TM}/Turbo code features several different types of space discretizations. All the FINE^{TM}/Turbo results presented in the remainder of this article have been computed by selecting the same spatial discretization of the convective terms used by the ISAAC code. The time-integration strategy of FINE^{TM}/Turbo is explicit and is based on Runge–Kutta integration accelerated by a full multigrid algorithm and implicit residual smoothing. As for turbulence modelling, FINE^{TM}/Turbo also features a large set of algebraic, one- and two-equation linear and non-linear differential turbulence models. However, at the time this manuscript is being prepared, transition from laminar to turbulent boundary layer can be prescribed only when using the one-equation Spalart–Allmaras (SA) turbulence model [**20**], which also allows integration all the way down to the wall without using wall functions. For this reason, all FINE^{TM}/Turbo results presented in this article have been determined by using this turbulent closure model. The FINE^{TM}/Turbo solver also features low-speed preconditioning to deal with low-speed flows. This option, however, was not used in the present study for reasons provided in the next section.

4 EFFECTS OF WAKE TRACKING AND TRANSITION MODELLING

In this section, we assess the improvement of the wake resolution achieved by using the wake tracking approach discussed in the section 2, and we also highlight the importance of taking into account the laminar-to-turbulent transition by comparing the aerofoil frictional parameters obtained by using either fully turbulent or transitional turbulence modelling.

To highlight the generality of the following findings, we have conducted all the analyses presented in this section using both ISAAC and FINE^{TM}/Turbo with the same computational grids. Unfortunately, at the time this manuscript is being prepared, ISAAC and FINE^{TM}/Turbo do not feature a common turbulence model that allows enforcing the position where transition from laminar to turbulent flow occurs. For this reason, all ISAAC results reported in this section use the low Reynolds number K–ε ASM model, whereas all FINE^{TM}/Turbo results have been obtained using the SA turbulence closure.

The test case we consider is the flow field of the FFA-W3-241 WT aerofoil. Experimental measurements of the flow field past this aerofoil have been performed for a free-stream Mach number of 0.11 and a Reynolds number of 1.6×10^6, and for several values of free-stream incidences. Steady and unsteady flow regimes have been analysed. The wind tunnel is of the

closed return type, and features an open test section with a cross-section of 7.5×7.5 m and a length of 10.5 m. The aerofoil model is lodged in a stand placed in the tunnel test section. The aerofoil model has a span of 1.9 m and a chord of 0.6 m giving an aspect ratio of 3.17, and is mounted 1.7 m from the tunnel floor and 3.2 m from the nozzle outlet. Endplates are fixed to the stand at the ends of the aerofoil model to limit 3D effects. The interested reader is referred to reference [**12**] for additional information on the experimental set-up and the wind tunnel corrections adopted in the postprocessing of the measured data.

This section considers the steady regime associated with an incidence of 4.02°. Note that no low-speed preconditioning has been used in any of the numerical simulations reported in this article. This has been done because initial numerical investigations have shown that the differences between the results obtained with low-speed preconditioning and those obtained without it are negligible for this fully attached flow regime.

Preliminary mesh sensitivity and refinement analyses have led to the choice of a C-grid with the following features: number of nodes past the aerofoil $I_{bb} = 301$, minimum distance from the aerofoil surface in chord units $dn = 5 \times 10^{-7}$, number of nodes in the normal direction $j_{max} = 129$, and number of nodes in C-cut $I_{bc} = 81$. The overall number of points on the C-lines is thus $I_{max} = 461$ so that this grid has an overall number of points of $N_{node} = 59\,469$. The far-field boundary is located about 20 chords away from the aerofoil in all directions. This grid has been generated in two versions: one featuring a straight horizontal C-cut (option 1), and the other featuring a user-given cut geometry (option 3) based on the near-field wake pattern obtained with an XFOIL analysis. These two meshes have the same number of nodes. The topological difference between these grids is the same as that between those of Figs 3 and 4.

The ISAAC flow analysis based on the K–ε ASM model for an incidence $\alpha = 4.02°$ has led to a maximum y^+ of 1.7 using either grid topology. The FINE^{TM}/Turbo flow analysis based on the SA model for the same incidence has led to a maximum y^+ of 1.4 using either grid topology. This highlights that the selected wall distance is adequate for resolving the aerofoil boundary layers. The contours of total pressure obtained by using the standard and adapted grids are reported in Figs 6 and 7, which refer to the ISAAC and FINE^{TM}/Turbo results, respectively. The definition of the total pressure coefficient is

$$C_{p^0} = \frac{p_{0,\infty} - p_0}{q_\infty}$$

where $p_{0,\infty}$ and p_0 denote the free-stream and local total pressure, respectively, and q_∞ is the free-stream dynamic head. The results of Figs 6 and 7 show that the wake resolution of both simulations with adapted

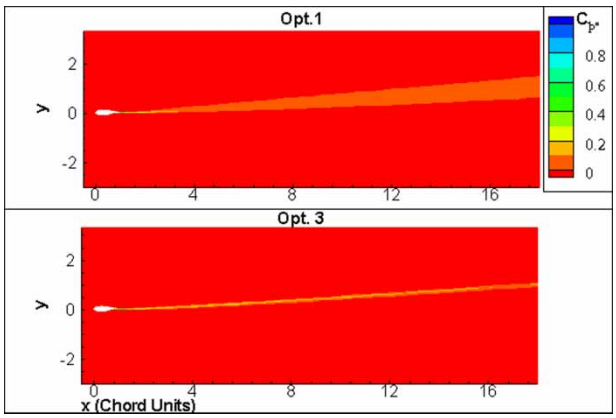

Fig. 6 Contours of total pressure coefficient computed using the ISAAC code with standard grid (option 1) and wake adapted grid (option 3) for $\alpha = 4.02°$

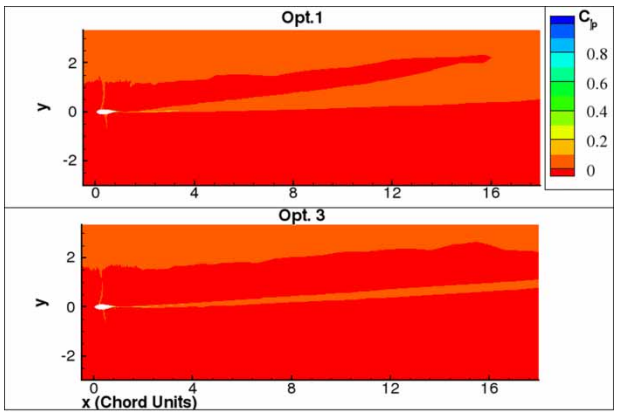

Fig. 7 Contours of total pressure coefficient computed using the FINE^{TM}/Turbo code with standard grid (option 1) and wake-adapted grid (option 3) for $\alpha = 4.02°$

grid (option 3) has substantially improved with respect to that achieved by using the standard grid (option 1). In the former case, in fact, the wake is significantly sharper and less diffused than in the latter. As for the comparison between the two codes with the adapted grid, it appears that for this incidence, ISAAC with the K–ε ASM model yields slower wake decay than FINE^{TM}/Turbo with the SA model. These observations are quantified in Figs 8 and 9, which report the total pressure coefficient at 1, 3, 5, 7, 9, and 11 chord lengths after the TE, computed with both codes. The sequence displayed in Fig. 8, which refers to the ISAAC/K–ε ASM solution, shows that the solution of the grid with straight horizontal cut has already a very diffused (shallow) trace of the wake at 7 chords from the TE, whereas the solution of the adapted grid still features a physically much more likely sharp wake at 11 chord lengths behind the TE. A similar trend is displayed by the FINE^{TM}/Turbo/SA solution (see Fig. 9). Despite the wake tracking feature, however, this solution predicts

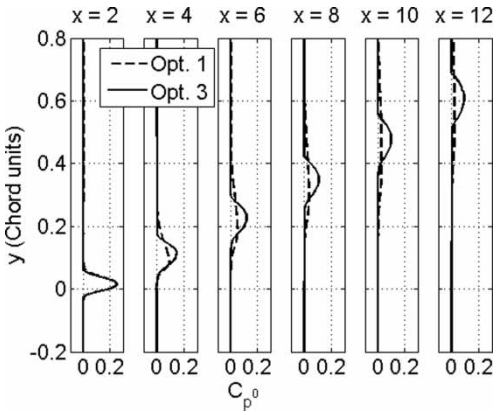

Fig. 8 Comparative analysis of wake evolution computed with standard (option 1) and wake-adapted (option 3) grid for $\alpha = 4.02°$, ISAAC/k–ε ASM solution

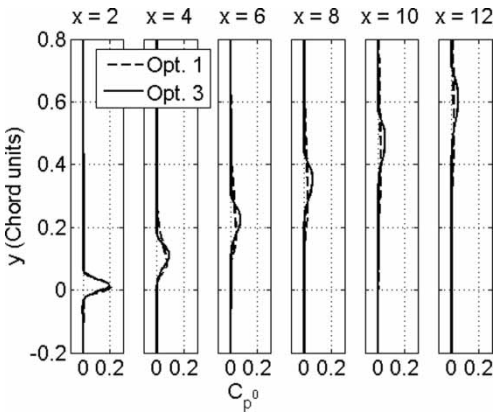

Fig. 9 Comparative analysis of wake evolution computed with standard (option 1) and wake-adapted (option 3) grid for $\alpha = 4.02°$; FINE^{TM}/Turbo/SA solution

a less pronounced total pressure loss and diffuses the wake more quickly than the ISAAC/K–ε ASM solution.

The alignment of the wake and the C-cut also has an impact on the convergence rate of the CFD run. This effect is particularly pronounced in the case of the ISAAC solver. The four subplots of Fig. 10 present the convergence history of the continuity, x- and y-components of the momentum, and energy equations obtained by using the grid with straight horizontal cut (option 1), that with straight rotated cut (option 2) and that with wake-adapted cut (option 3). One sees that the worst convergence rate is obtained with the option 1 grid. In this case, the maximum flow residuals occur in the wake shortly after the TE in the area where the wake leaves the high-refinement area past the C-cut. A better convergence rate is obtained with the rotated cut (option 2), but the best rate is achieved with the wake-adapted grid.

The corresponding plots referring to the FINE^{TM}/Turbo analyses are displayed in Fig. 11. With this

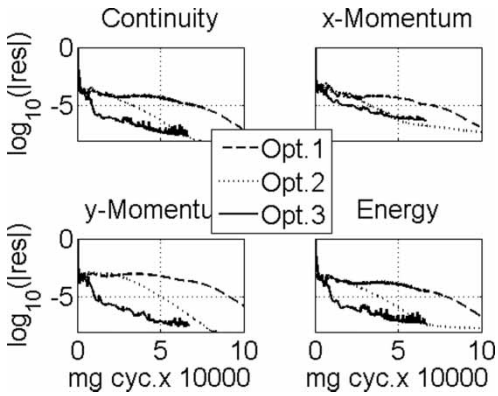

Fig. 10 Convergence histories of the ISAAC CFD solver with option 1, option 2, and option 3 grids for $\alpha = 4.02°$

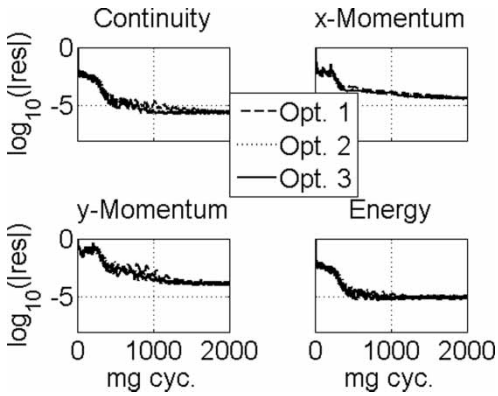

Fig. 11 Convergence histories of the FINE^{TM}/Turbo CFD solver with option 1, option 2, and option 3 grids for $\alpha = 4.02°$

solver the effect of the wake-grid alignment on the convergence rate is far less pronounced, convergence being only marginally faster on the wake-adapted grid. Note, however, that the two solvers adopt radically different integration procedures and different multigrid settings. This explains why FINE^{TM}/Turbo achieves convergence using two orders of magnitude fewer multigrid cycles than the ISAAC solver. It should also be observed that the ISAAC simulation features a two-equation turbulence model, whereas that of FINE^{TM}/Turbo uses a one-equation turbulence model. This is one additional reason why the cost of an ISAAC multigrid iteration cannot be compared with that of a FINE^{TM}/Turbo multigrid iteration. A code-to-code comparison in terms of computational efficiency is, however, beyond the scope of the present analysis.

These observations highlight that this adaptation strategy not only improves the resolution of the flow field, but it may also improve the convergence properties of the CFD solver, depending on the robustness of the integration process and presumably also on specific mathematical features of the turbulence model at hand.

Both codes allow enforcing of the chordwise position where the laminar-to-turbulent transition occurs. This feature has been exploited in the present analyses. The chordwise position of the transition on both aerofoil sides has been determined by the same XFOIL analysis used to determine the cut geometry for WINGRID. These transition positions have been used as input for both the ISAAC and FINE^{TM}/Turbo analyses, and all results presented thus far have been computed with such a transitional set-up. Figure 12 provides the skin-friction coefficient on the aerofoil surface predicted respectively by the transitional ISAAC analysis (curves labelled 'trns') with the standard (option 1) and wake-adapted (option 3) grids. Figure 13 provides instead the corresponding data obtained by means of the FINE^{TM}/Turbo analysis. The XFOIL result is also shown in both figures for comparison. First, note that the transitional RANS profiles computed by using either codes with the standard and wake-adapted grids present negligible differences. This seems to indicate that, for this flow regime, the extent to which we resolve the wake has negligible impact on the prediction of the drag computed by surface integration of the viscous stress. It should be noted, however, that this conclusion will most likely not hold for flow fields, which, unlike that considered here, have a significant level of flow unsteadiness. Figure 12 also shows that both ISAAC/K–ε ASM transitional profiles and the XFOIL profile show a sudden rise of C_f at about 35 per cent chord on the upper side and about 45 per cent on the lower side. These are the positions at which transition occurs. The sharp increment of viscous stress is caused by the fact that the wall viscous stress in the turbulent boundary layer is higher than that in the laminar boundary layer preceding the transition. The FINE^{TM}/Turbo transitional SA results displayed in Fig. 13 show a smoother rise in C_f at both transition locations along with less pronounced maximum and minimum values in their immediate neighbourhood. Within the fully turbulent boundary layer that develops downstream of both transition locations, the skin-friction levels predicted by FINE^{TM}/Turbo/SA are in good agreement with the XFOIL prediction, whereas the ISAAC/K–ε ASM analysis overestimates C_f with respect to the XFOIL prediction. Since no experimental data are available for the skin-friction coefficient, it is hard to establish which of the three computational results is more reliable.

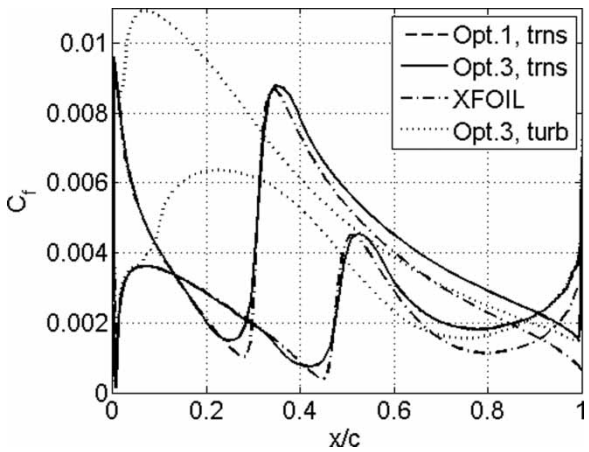

Fig. 12 ISAAC computed profiles of skin-friction coefficient for $\alpha = 4.02°$

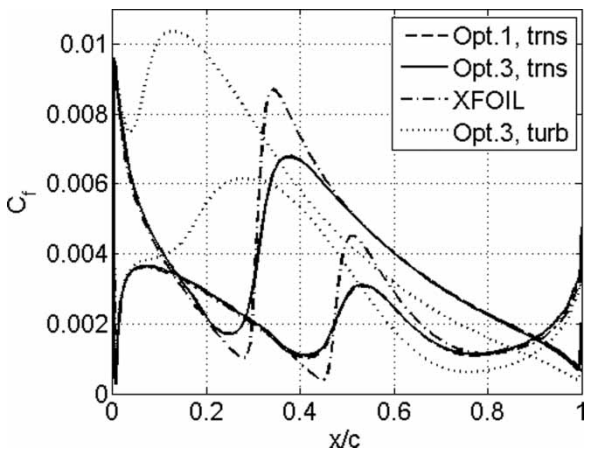

Fig. 13 FINE^{TM}/Turbo computed profiles of skin-friction coefficient for $\alpha = 4.02°$

Figures 12 and 13 also report the C_f profiles obtained with a fully turbulent RANS analysis (curve labelled 'turb'). With both codes, the fully turbulent RANS analysis yields significantly higher drag levels than the transitional analysis, due to the substantially higher level of C_f that it attributes to the front part of the aerofoil boundary layers. As shown later in this section, the drag coefficient computed by the transitional analysis is closer to the measured value. There is also evidence that the boundary layers past this type of aerofoil are indeed transitional. For example, the experimental data of the flow field past the S809 aerofoil, a 21 per cent thick WT aerofoil with geometry very close to that of the FFA-W3-241 aerofoil and tested for Reynolds and Mach number very close to those of the present study, show that the boundary layer is transitional on both aerofoil sides for an angle of attack varying between $-2°$ and $10°$. These data have been first published in reference [**21**], which reports that the experimental transition locations were obtained using a stethoscope. In reference [**5**], these experimental data are compared with several transitional CFD results (including XFOIL analyses), and a very good general agreement between measurements and simulations is observed. The transitional character of the boundary layers of thick and relatively low Reynolds number WT aerofoils and its impact on the aerodynamic forces point to the importance of modelling transition when using CFD for WT design.

Computed and measured profiles of static pressure coefficient C_p are presented in Figs 14 and 15. The

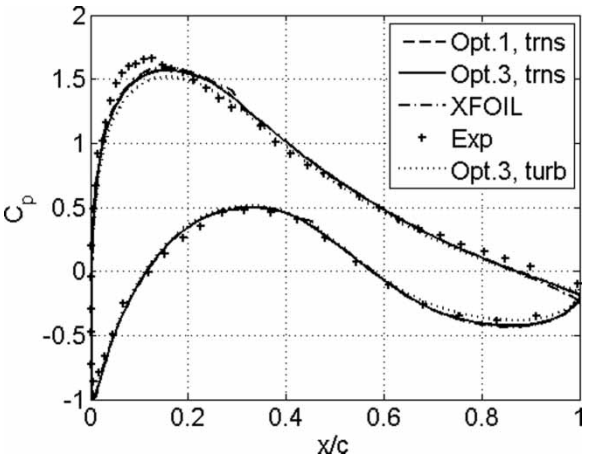

Fig. 14 ISAAC computed and measured profiles of static pressure coefficient for $\alpha = 4.02°$

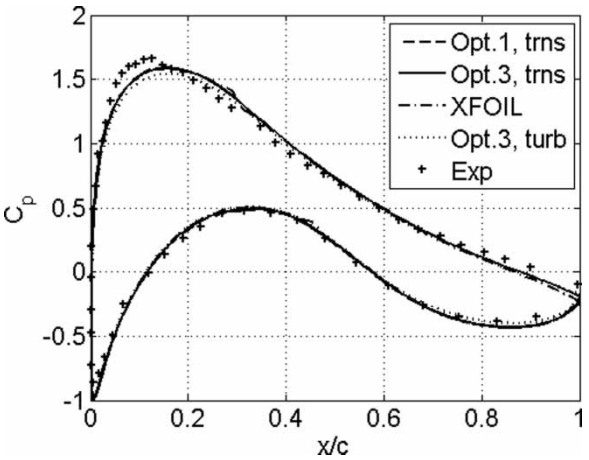

Fig. 15 FINE^{TM}/Turbo computed and measured profiles of static pressure coefficient for $\alpha = 4.02°$

definition of this parameter is

$$C_p = \frac{p - p_\infty}{q_\infty}$$

where p_∞ and p denote the free-stream and local static pressure, respectively. Both in the case of ISAAC (Fig. 14) and FINE^{TM}/Turbo (Fig. 15), one sees that (a) there are no visible differences between the transitional results obtained with the standard and adapted grid, (b) these two transitional RANS results and the XFOIL prediction are in excellent agreement, and (c) the CFD profile obtained with a fully turbulent analysis deviates from all transitional numerical results in the first 35 per cent of the upper side, where transitional analyses place the transition. The difference between transitional and fully turbulent profiles on the lower side is very small. As for the comparison between measured and computed data, some differences between all computed transitional results and the experimental data are visible in the front and rear parts of the upper side. The fact that the RANS and XFOIL profiles present negligible differences despite the fact that they use substantially different flow models makes it possible to assume that some neglected wind tunnel effects may be responsible for the aforementioned differences.

As reported in reference [**12**], measurements of the total pressure in the wake were also made. A fixed vertical rake of pressure taps was positioned behind the aerofoil. The variation of the flow incidence was enabled by rotating the aerofoil about a hinge placed at 40 per cent of its chord. The distance between the TE and the wake rake of the aerofoil was 70 per cent chord lengths when the aerofoil was in the horizontal position. The measured profile of total pressure coefficient in the wake and that computed by ISAAC and FINE^{TM}/Turbo using the wake-adapted grids are compared in Figs 16 and 17, respectively. The overall agreement between depth and width of computed and measured profiles is fairly good. The centreline of the computed profile appears to have a left offset with respect to the measured profile. Conversely, the position of the TE streamline predicted by XFOIL is closer to the centreline of the measured wake. This comparison is affected by some uncertainty, such as the effects of top and bottom tunnel walls on the streamline curvature at the inlet of the test chamber. As reported in reference [**12**], these effects are only partially taken into account in the experimental corrections.

The effect of the grid adaptation on the wake resolution for $\alpha = 4.02°$ is not significant within one chord length from the TE (Figs 8 and 9). Hence the profiles computed with the option 1 grid do not differ from the computed profiles displayed in Figs 16 and 17.

The numerical and experimental values of lift coefficient C_L and drag coefficient C_D are reported in Tables 1 and 2 for the ISAAC and FINE^{TM}/Turbo analyses, respectively. All numerical values are obtained by integrating pressure force and viscous stress on

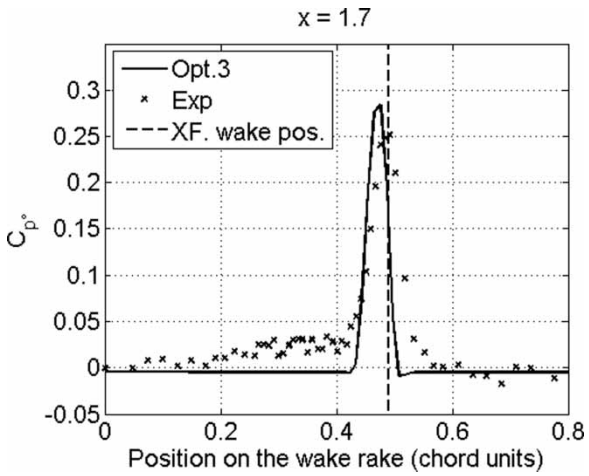

Fig. 16 Measured and computed (ISAAC/k–ε) ASM profiles of total pressure coefficient behind the aerofoil TE for $\alpha = 4.02°$

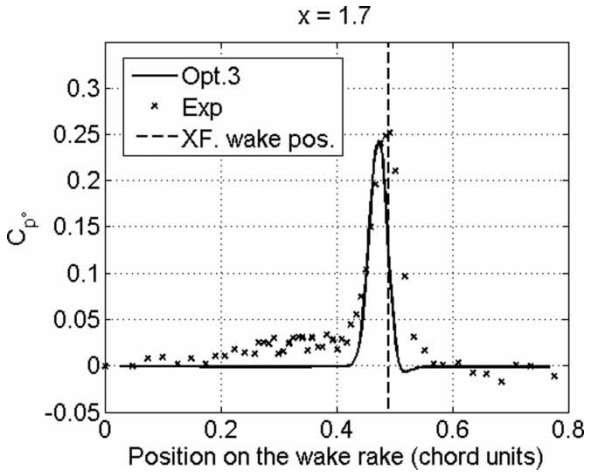

Fig. 17 Measured and computed (FINE™/Turbo/SA) profiles of total pressure coefficient behind the aerofoil TE for $\alpha = 4.02°$

the aerofoil surface. The experimental estimate of the forces is instead obtained by integrating the measured static pressure distribution on the aerofoil, and applying a momentum balance approach to a control volume enclosing the aerofoil. The momentum balance calculation makes use of the wake rake data. Further details on the calculation of the forces based on the experimental data are provided in reference [**12**]. The first two columns of Tables 1 and 2 report C_L and C_D computed by transitional RANS analyses with the standard and adapted grids, respectively; the third column has the force coefficients computed by the fully turbulent RANS analyses with adapted grid, and the last two columns have the XFOIL and experimental estimates, respectively. One notices that: (a) both in the case of ISAAC and FINE™/Turbo, the mesh adaptation in the wake region has a negligible effect on the drag force, and a small effect (variation of about 0.5 per cent) on the lift force; (b) both in the case of ISAAC and FINE™/Turbo, the error induced by not accounting for laminar-to-turbulent transition is about 7 per cent for the lift and 50 per cent for the drag; (c) the lift predicted by the transitional CFD analyses are in reasonably good agreement with experimental data, and the level of agreement is slightly worse than that between XFOIL and the experimental data; and (d) the drag predicted by the transitional CFD analyses are closer than the XFOIL prediction to the experimental value.

Table 1 Measured and computed force coefficients (ISAAC/K–ε ASM CFD analyses) for $\alpha = 4.02°$

	Option 1 – Trns	Option 3 – Trns	Option 3 – Turb	XFOIL	Exp
Cl	0.7596	0.7549	0.7006	0.7691	0.769
Cd	0.0114	0.0113	0.0169	0.0093	0.0126

Table 2 Measured and computed force coefficients (FINE™/Turbo /SA CFD analyses) for $\alpha = 4.02°$

	Option 1 – Trns	Option 3 – Trns	Option 3 – Turb	XFOIL	Exp
Cl	0.7778	0.7712	0.7295	0.7691	0.769
Cd	0.0100	0.0102	0.0146	0.0093	0.0126

5 EFFECTS OF TURBULENCE MODELLING

To assess the influence of turbulence modelling on the computed forces, the flow field past the FFA-W3-241 aerofoil for $\alpha = 10.2°$ has been computed using the linear and ASM versions of both the K–ω and the K–ε models. This analysis has only been performed by means of the ISAAC code, because at present the FINE™/Turbo code allows the user to specify the position of the laminar-to-turbulent transition only with the SA model.

The skin-friction coefficient computed with all four turbulence models is plotted in Figs 18 and 19. Overall, the best agreement between XFOIL and ISAAC is obtained with the K–ω ASM model. On the upper side, some deviations between these two results are only observed from 70 per cent chord to the TE. At present, it is not clear why both K–ω models appear not to trigger the laminar-to-turbulent transition at the same positions of XFOIL. These latter have been prescribed as input for all four calculations, but only the two K–ε analyses appear to place the transition exactly where required.

Figures 20 and 21 depict the static pressure coefficient determined by all four CFD analyses and XFOIL, and show that the differences among all results are negligible.

The total pressure deficit in the wake computed by using the four turbulence models is compared to the

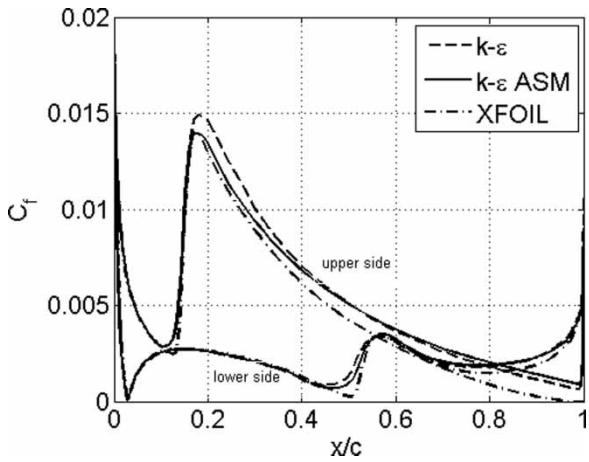

Fig. 18 Comparative analysis of turbulence models for $\alpha = 10.2°$: skin-friction coefficient computed with K–ε and K–ε ASM models

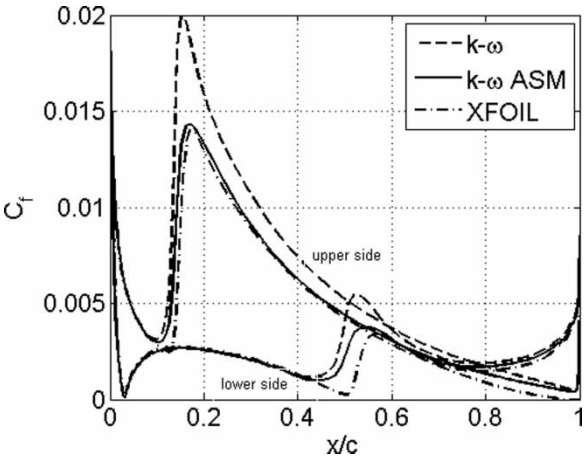

Fig. 19 Comparative analysis of turbulence models for $\alpha = 10.2°$: skin-friction coefficient computed with K–ω and K–ω ASM models

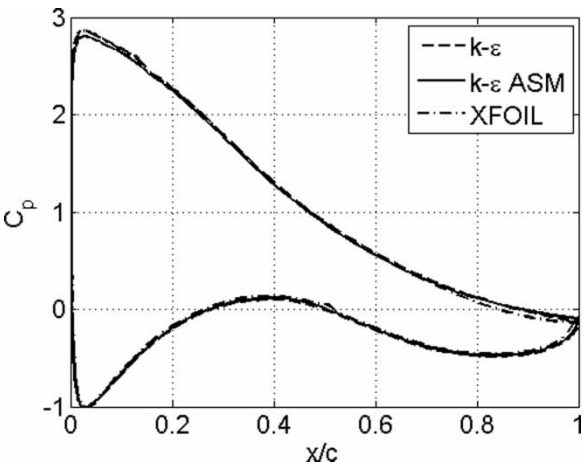

Fig. 20 Comparative analysis of turbulence models for $\alpha = 10.2°$: pressure coefficient computed with K–ε and K–ε ASM models

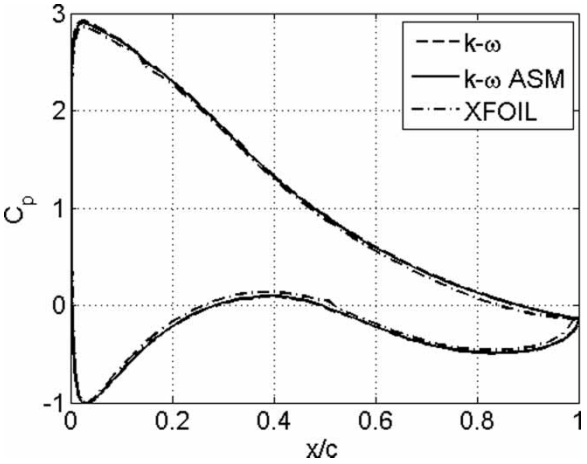

Fig. 21 Comparative analysis of turbulence models for $\alpha = 10.2°$: pressure coefficient computed with K–ω and K–ω ASM models

wake rake data in Figs 22 and 23. The most remarkable differences between the K–ε and K–ω models are that (a) the former ones predict a minimum total pressure in the wake, which is about 25 per cent lower than the predictions of the latter models, and (b) the width of the wake predicted by the K–ω models is slightly larger than the width computed by the other two models. Both features appear to make the prediction of the K–ω models closer to the experimental data. On the other hand, the use of either the linear eddy viscosity model associated with the Boussinesq approximation or the ASM expression of the Reynolds stress tensor seems to make little difference for both K–ε and K–ω models. This is highlighted by the fact that there are small differences between the two profiles of Fig. 22, and also between those of Fig. 23. Finally,

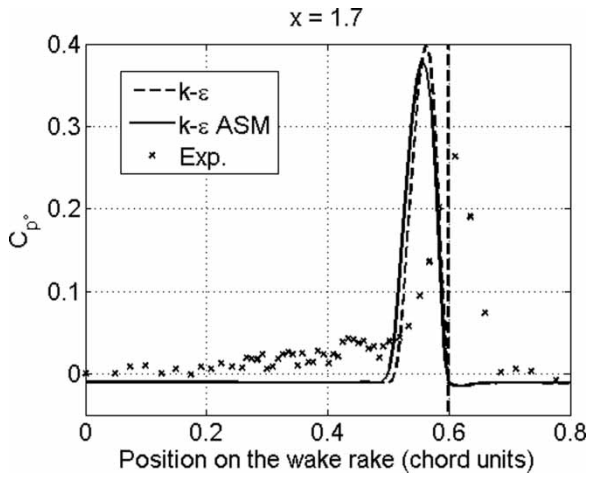

Fig. 22 Comparative analysis of total pressure coefficient at 70 per cent chord from TE using different turbulence models for $\alpha = 10.2°$: profiles computed by K–ε and K–ε ASM models

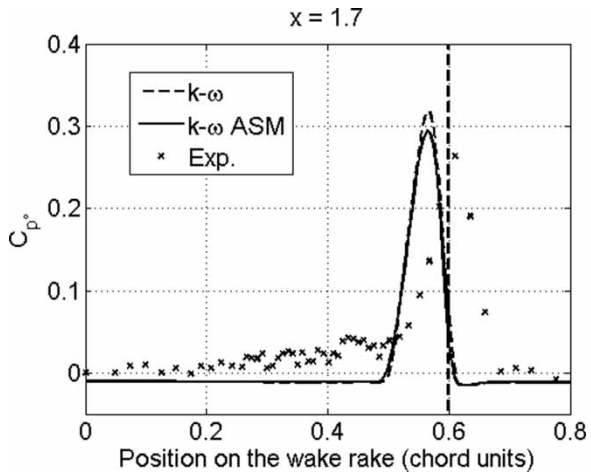

Fig. 23 Comparative analysis of total pressure coefficient at 70 per cent chord from TE using different turbulence models for $\alpha = 10.2°$: profiles computed by K–ω and K–ω ASM models

Table 3 Measured and computed force coefficients (option 3 grid) for $\alpha = 10.2°$ using four different turbulence models and the ISAAC code

	k–ε	k–ε ASM	k–ω	k–ω ASM	Exp.
Cl	1.4296	1.3949	1.4633	1.4495	1.344
Cd	0.0194	0.0204	0.0197	0.0184	0.0171

the computed force coefficients using the four models are reported in Table 3. The best prediction of the lift force seems to be that of the K–ε ASM model, whereas the best drag prediction appears to be that of the K–ω ASM model. It should be observed that the experimental values of lift and drag coefficients have been obtained using different methods (lift by aerofoil pressure integration and drag by using wake rake data for momentum balance). Hence it is possible that the two experimental forces may be affected by different types and levels of uncertainties, which probably explains why the best prediction of lift and drag appear to be given by two different analyses.

6 CONCLUSIONS

This study has presented an *a priori* grid tailoring method for structured grids aimed at quantifying the improvement of the resolution of the wake shed by WT aerofoils achievable by grid adaptation. To assess the generality of the reported findings, an open source and a commercial RANS codes have been used. The latter has been used with the one-equation SA turbulence model and the former with several two-equation models. Using either analysis set-up, the resolution of the wake shed at the trailing edge of a typical wind turbine aerofoil for an incidence of 4.02° appears to improve with wake-tracked grids, though such improvement seems to be higher for the open source code. This is most likely due to the use of different turbulence models in the two solvers. Indeed, similar studies performed by the authors but not reported herein suggest that the extent of the sensitivity of the wake resolution to the grid refinement in the wake region using a given CFD solver greatly depends on the choice of the turbulence model. More precisely, the sensitivity is higher when using two- rather than one-equation turbulence models. Additionally, the improvement of the wake resolution achieved by wake tracking becomes more significant as the thickness of the wake grows, and this condition is associated with higher values of the flow incidence. Indeed, the analyses for higher incidence ($\alpha = 10.2°$) reported in reference [**22**] show that the wake has nearly disappeared within three chords from the TE when using a standard C-grid. Conversely, the same physical wake is preserved as far as 20 chords from the TE, when the wake-tailored grid is adopted. The wake-adapted grid has also been found to improve the convergence characteristics of the CFD calculations. As for the computed lift and drag coefficients, these unexpectedly appear to be fairly insensitive to the grid resolution.

The extent of the wake resolution enhancement achievable by grid adaptation has a great potential for supporting the application of mid-field drag calculations. Since a substantially higher flow resolution can be obtained by simply adapting the grid without changing the grid size, it also points to the fact that grid-adaptation and high-order methods should be both considered for the development of optimal RANS solvers.

The numerical analyses presented in this article refer to 2D attached flows. The proposed wake-tracking algorithm can be generalized in a straightforward fashion to 3D attached flow problems by incorporating a 3D potential flow solver into the grid generation process. Because of the extremely low computational cost of the potential equations solver, this feature would have a negligible impact on the computational cost of the grid generation. In the case of 2D and 3D flows with large amounts of separation, the wake-tracking algorithm may yield smaller resolution enhancements than in the case of attached flows, as large vortex trails may also be found farther away from the C-cut. Enhancements of the presented method, or alternatively, a computationally more costly dynamic grid adaptation, might have to be considered in these circumstances.

The comparison of transitional and fully turbulent analyses reveals that the errors on the aerodynamic forces introduced by not accounting for transition are of the order of 10 per cent for the lift and 50 per cent for the drag force.

The comparative analysis of four two-equation turbulence models shows large variations of the four predicted drag coefficients, with the K–ω ASM result appearing to be the closest to the measured data.

ACKNOWLEDGEMENTS

The authors would like to thank Gaia-Wind Ltd for contributing to the realization of this study, and the Risoe National Laboratory for providing the geometry and the experimental data of the FFA-W3-241 aerofoil. This research has been carried out in the framework of a project supported by the Engineering and Physical Sciences Research Council under grant number EP/F038542/1.

REFERENCES

1 **Bertagnolio, F., Sorensen, N. N.,** and **Rasmussen, F.** New insight into the flow around a wind turbine aerofoil section. *Sol. Energy Eng.*, 2005, **127**, 214–222.

2 **Stone, C. P., Tebo, S. M.,** and **Duque, C. P. N.** Fluid dynamics of flatback aerofoils for wind turbine applications. AIAA paper no. 2006-194, 2006.

3 **Le Pape, A.** and **Lecanu, J.** 3D Navier–Stokes computations of a stall-regulated wind turbine. *Wind Energy*, 2004, **7**, 309–324.

4 **Wolfe, W. P.** and **Ochs, S. S.** CFD calculations of S809 aerodynamic characteristics. AIAA paper no. 07-0973, 1997.

5 **Langtry, R. B., Gola, J.,** and **Menter, F. R.** Predicting two-dimensional aerofoil and 3D wind turbine rotor performance using a transitional model for general CFD codes. AIAA paper no. 2006-395, 2006.

6 **Wilcox, D. C.** Reassessment of the scale-determining equation for advanced turbulence models. *AIAA J.*, 1988, **26**, 1299–1310.

7 **Menter, F. R.** Two-equation eddy-viscosity turbulence models for engineering applications. *AIAA J.*, 1994, **32**, 1598–1605.

8 **Paparone, A.** and **Tognaccini, R.** Computational fluid dynamics-based drag prediction and decomposition. *AIAA J.* 2003, **41**, 1647–1657.

9 **Fletcher, T. M.** and **Brown, R. E.** Simulating wind turbine interactions using the vorticity transport equations. In Proceedings of the 28th ASME Wind Energy Symposium, Orlando, January 2009.

10 **Habashi, W. G., Dompierre, J., Bourgaulta, Y., Ait-Ali-Yahiaa, D., Fortin M.,** and **Vallet, M.-G.** Anisotropic mesh adaptation: towards user-independent, mesh-independent and solver-independent CFD. Part I: general principles. *Int. J. Numer. Methods Fluids*, 2000, **32**, 725–744.

11 **Wang, Z. J.** High-order methods for the Euler and Navier–Stokes equations on unstructured grids. *Progr. Aerosp. Sci.*, 2007, **43**, 1–41.

12 **Fuglsang, P., Antoniou, I., Dahl, K. S.,** and **Madsen, H. A.** Wind tunnel tests of the FFA-W3-241, FFA-W3-301 and NACA-63-430 aerofoils, Technical report R-1041(EN), Riso National Laboratory, Denmark, 1998.

13 **Morrison, J. H.** A compressible Navier–Stokes solver with two-equation and Reynolds stress turbulence closure models. NASA CR4440, 1992.

14 **Drela, M.** An analysis and design system for low Reynolds number airfoils. In *Lecture notes in engineering* (Ed. T. J. Mueller), vol. 54, 1989, pp. 1–12 (Springer, New York).

15 **Drela, M.** and **Giles, M.** Viscous-inviscid analysis of transonic and low Reynolds number airfoils. *AIAA J.*, 1987, **25**, 1347–1355.

16 **Foerster, M.** and **Campobasso, M. S.** Development of a hyperbolic grid generation code and viscous CFD analysis of wind turbine aerofoils, Technical report 0802, Department of Aerospace Engineering, University of Glasgow, UK, 2008.

17 **Guerri, O., Bouhadef, K.,** and **Harhd, A.** Turbulent flow simulation of the NREL S809 aerofoil. *Wind Eng.*, 2006, **30**, 287–302.

18 **Zhang, H. S., So, R. M. C., Gatski, T. B.,** and **Speziale, C. G.** *A near-wall second-order scheme for compressible turbulent flows, near-wall turbulent flows* (Eds R. M. C. So, C. G. Speziale, and B. R. Launder), 1933 (Elsevier Science Publishers, Amsterdam).

19 **Gatski, T.** and **Speziale, C.** On explicit algebraic stress models to compute turbulent flows. *J. Fluid Mech.*, 1993, **254**, 59–78.

20 **Spalart, P. R.** and **Allmaras, S. R.** A one-equation turbulence model for aerodynamic flows. *Rech. Aérosp.*, 1994, **1**, 5.

21 **Somers, D. M.** Design and experimental results for the S809 airfoil, Technical report NREL/SR-440-6918, National Renewable Energy Laboratory, Colorado, USA, 1997.

22 **Campobasso, M. S., Zanon, A., Foerster, M., Fraysse, F.,** and **Bonfiglioli, A.** CFD modelling of wind turbine aerofoil aerodynamics. 63° Congresso Nazionale ATI Energia per lo Sviluppo Sostenibile, Palermo, Italy, 23–26 September 2008.

APPENDIX

Notation

C_D	drag coefficient
C_f	skin-friction coefficient
C_L	lift coefficient
C_{p^0}	total pressure coefficient
C_P	static pressure coefficient
p	static pressure
p_∞	free-stream static pressure
$p_{0,\infty}$	free-stream total pressure
p_0	total pressure
q_∞	free-stream dynamic head
α	angle of attack